Journal of Corrosion and Materials
www.corromat.com

J. Corros. Mater. (2025) 4(2), 195–205.

A Process-Window and Saturation-Kinetics Framework for pH-Controlled Permanganate Decontamination of 304L Stainless Steel

Joshua O. Atiba[1,*]

Department of Mechanical Engineering, Bells University of Technology, P.M.B. 1015, Ota, Ogun State, Nigeria

*Corresponding author: atibajoshua7@gmail.com

(Received: 16 August 2025. Received in revised form: 17 November 2025. Accepted: 28 November 2025. Published online: 30 December 2025.)

Abstract

Permanganate-based oxidizing steps are widely applied in nuclear chemical decontamination to oxidize chromium-rich oxides prior to reductive dissolution; however, the oxidizing-step pH strongly influences passive-film stability and substrate metal loss. This paper develops a quantitative process-window framework for 304L stainless steel exposed to 1 g/L $KMnO_4$ solutions spanning acidic (HNO_3-adjusted) and alkaline (NaOH-adjusted) regimes. Using published mass-loss trends, polarization behavior, and SEM morphology as constraints, we formalize a corrosion–efficacy trade space and introduce a compact saturation-kinetics model for oxide removal on preoxidized 304L. A reanalysis of the reported alkaline cycling dataset at 0.4 g/L NaOH demonstrates rapid convergence of cumulative mass loss (0.161, 0.256, 0.351, 0.354, 0.358 mg/cm^2 for cycles 1–5), consistent with finite oxide inventory removal followed by negligible incremental loss. We interpret the observed microspore morphology and subsequent reoxidation tendency as a surface-state consequence of porous residual structure that can accelerate oxide nucleation during post-treatment thermal exposure. The resulting process-window concept provides a practical basis for selecting oxidizing-step pH and minimum cycle count to achieve oxide removal while limiting corrosion allowance consumption.

Keywords: Mappings, convergence, hyperbolic spaces, iteration process.

1. Introduction

Chemical decontamination is routinely employed in nuclear power plants to reduce circuit dose rates prior to inspection, repair, and component replacement activities [1, 2]. During normal operation, corrosion and wear processes generate particulate and adherent oxide deposits on primary-system materials [3]. These deposits not only act as sinks for transition metals such as Fe, Ni, and Co, but also concentrate activated radionuclides (e.g., Co-bearing species) through transport, deposition, and incorporation mechanisms [4, 5]. As a consequence, accumulated oxides can become a major contributor to shutdown dose fields, motivating chemical cleaning campaigns that dissolve deposits and mobilize activity into controlled waste streams [1, 2].

A persistent technical difficulty is that the oxide deposits formed on stainless steels and Ni-based alloys in high-temperature water are typically heterogeneous, multi-layered, and often enriched in chromium near the metal/oxide interface [6, 7]. In pressurized-water reactor chemistry, for instance, mixed spinel-type oxides may coexist with Cr-rich inner layers that exhibit comparatively low solubility in many reducing or chelating formulations [3, 8]. Since chromium commonly exists as Cr(III) in these oxides, its dissolution kinetics can be sluggish unless it is oxidized to higher-valence, more soluble species [9]. This chromium barrier is a central reason why many industrial decontamination procedures employ an oxidizing pretreatment step to condition the deposit prior to a subsequent reducing/complexing dissolution stage [1, 2].

Permanganate-based oxidizing steps have therefore been widely adopted as practical pretreatments because permanganate is a strong oxidant over a broad range of pH and can oxidize Cr(III) in chromium-containing oxides, thereby increasing oxide solubility in the following reduction stage [10, 11]. In typical process logic, the oxidizing step modifies the oxide chemistry and disrupts the integrity of chromium-enriched regions, after which a reducing agent (often combined with complexants or organic acids) dissolves the modified oxide and stabilizes dissolved metal ions [2, 1]. However, this benefit comes with a key operational concern: the same oxidizing environment that targets deposit oxides can also affect the substrate alloy by altering passive-film composition, destabilizing protective layers, and accelerating metal loss [9, 12]. For stainless steels such as 304L, maintaining passivity is essential because protective behavior relies on a stable Cr-rich passive film whose integrity depends strongly on solution chemistry, redox potential, and pH [12].

Among controllable parameters, pH plays a particularly influential role because it simultaneously governs (i) the oxidizing power and speciation of permanganate and its reduction products, (ii) the dissolution kinetics of oxide phases, (iii) the stability domain of stainless-steel passivity, and (iv) the likelihood of localized breakdown phenomena [13, 9]. Acidified permanganate solutions may promote rapid oxide attack but can also narrow or destroy the passive region, increasing

uniform and localized corrosion risk [12]. Conversely, alkaline permanganate can preserve passivity more effectively, yet excessive alkalinity may introduce new instability by shrinking the passive potential range or altering film properties in ways that increase dissolution [13]. These competing tendencies imply that decontamination chemistry should be approached as an optimization problem rather than a monotone choice of "stronger oxidant" or "more alkaline is safer" [2]. In practice, plant engineers must balance oxide-removal completeness against corrosion allowance consumption, component life considerations, and process time constraints [1]. A decision framework that explicitly links pH selection and the number of oxidation–reduction cycles to measurable outcomes is therefore of direct practical value [2].

In addition to pH, cycle count itself is a critical and often under-optimized variable [11]. Oxide films have finite inventory: once the removable portion of the oxide is depleted, additional cycles are expected to yield diminishing returns in removal while still exposing the substrate to reactive chemistry [10]. This motivates the need for a quantitative representation of how oxide removal evolves with cycle number, including identification of a saturation point beyond which further cycling is inefficient or potentially harmful [2]. Moreover, post-treatment surface condition matters: even when oxide removal appears complete, surface roughening or micro-porosity generated during cycling can influence subsequent oxide nucleation and reoxidation when the component returns to high-temperature water [6, 7]. Thus, a comprehensive "process window" should account not only for immediate metal loss and oxide removal, but also for the surface state that governs reoxidation tendency [12].

This work advances prior comparative studies by translating reported mass-loss behavior, electrochemical polarization trends, and surface morphology observations into two complementary contributions. First, we formulate a process-window decision framework that organizes the corrosion–efficacy trade space under pH control of permanganate oxidizing steps, clarifying the operational consequences of acidic versus alkaline regimes and the nontrivial risk of extreme alkalinity. Second, we introduce a saturation-kinetics representation for oxide-film removal on preoxidized 304L stainless steel, providing a compact way to interpret rapid convergence of cumulative mass loss with cycle number and to define a practical stopping criterion for cycling. The intent is not to replicate experiments, but to deliver a predictive structure that can be adopted and strengthened by adding targeted measurements such as surface-chemistry depth profiling and electrochemical impedance spectroscopy, ultimately enabling decontamination procedures that are both effective and corrosion-conscious.

2. Process-Window Concept and Modeling

2.1 Trade-space definition

The oxidizing step in a permanganate-based decontamination cycle must be evaluated as a coupled, multi-objective design problem because the same chemistry that oxidatively destabilizes Cr-bearing deposits can also perturb the Cr-rich passive film that protects 304L stainless steel. For engineering selection of an operating envelope, we formalize a two-axis trade space in which the first axis represents *oxide-removal efficacy* and the second axis represents *substrate corrosion risk*. The intent is to convert qualitative statements such as "acidic permanganate is more aggressive" into quantitative decision rules that can be applied to cycle-count selection and pH targeting.

For clarity, Table 1 summarizes the principal quantities introduced in this section. The cycle index is $n \in \mathbb{N}$, and all masses are expressed per unit exposed area (mg/cm^2).

Table 1: Notation for process-window modeling.

Symbol	Meaning
pH	Oxidizing-step pH (controlled by HNO_3 or NaOH)
n	Number of oxidation–reduction cycles
$m(n)$	Measured cumulative mass loss after n cycles (mg/cm^2)
$m_{\mathrm{ox}}(n)$	Cumulative oxide-related mass removal after n cycles (mg/cm^2)
$m_{\mathrm{sub}}(n)$	Cumulative substrate metal loss after n cycles (mg/cm^2)
m_∞	Effective removable oxide inventory (mg/cm^2)
k	Effective per-cycle oxide depletion constant (cycle^{-1})
i_{corr}	Corrosion current density inferred from polarization (A/cm^2)
i_{pass}	Passive current density in the passive region (A/cm^2)
E_{pit}	Pitting/passivity breakdown potential (V vs reference)
E_{oc}	Open-circuit potential in the oxidizing step (V vs reference)

2.1.1 Decomposition of cumulative mass loss

For an oxide-bearing specimen, the cumulative mass-loss signal mixes two physically distinct contributions:

$$m(n) \;=\; m_{\mathrm{ox}}(n) \;+\; m_{\mathrm{sub}}(n), \tag{1}$$

where $m_{\mathrm{ox}}(n)$ represents depletion of deposit/film inventory (the desired decontamination effect) and $m_{\mathrm{sub}}(n)$ represents true dissolution of base metal (a cost or constraint). This decomposition is conceptually important even when the two components cannot be perfectly separated from gravimetry alone, because it clarifies why diminishing returns with n are expected once $m_{\mathrm{ox}}(n)$ saturates.

2.1.2 Efficacy metric

A normalized oxide-removal efficacy can be defined as the fraction of removable oxide inventory depleted after n cycles:

$$\eta(n) \;:=\; \frac{m_{\mathrm{ox}}(n)}{m_{\mathrm{ox}}(\infty)} \in [0,1], \qquad m_{\mathrm{ox}}(\infty) = m_{\infty}. \tag{2}$$

An operational objective is to achieve $\eta(n) \geq \eta_{\min}$ with the smallest feasible cycle count n while respecting corrosion constraints.

2.1.3 Risk metric and electrochemical linkage

A complementary risk quantity is the cumulative substrate loss $m_{\mathrm{sub}}(n)$, which can be linked to electrochemical currents through Faraday's law. For a metal dissolution process represented by an effective equivalent weight EW (g/equiv) and F the Faraday constant, the areal mass loss due to an average current density $i(t)$ over exposure time interval $[0,\tau]$ is

$$m_{\mathrm{sub}} \;=\; \frac{EW}{F} \int_0^{\tau} i(t)\, dt, \tag{3}$$

where m_{sub} is in g/cm^2 if EW is in g/equiv and i is in A/cm^2. Converting to mg/cm^2 multiplies the right-hand side by 10^3. In practice, polarization curves provide i_{corr} and characterize i_{pass} and the width of the passive region; these observables inform whether $m_{\mathrm{sub}}(n)$ is expected to grow mildly (stable passivity, low i_{pass}) or rapidly (passive breakdown, elevated currents). For decontamination design, a common constraint form is

$$m_{\mathrm{sub}}(n) \;\leq\; m_{\mathrm{allow}}, \tag{4}$$

where m_{allow} is a corrosion allowance set by component life and safety considerations.

2.1.4 Passivity stability as a probabilistic constraint

Beyond total mass loss, localized breakdown probability is central because a small number of breakdown events can dominate damage. A convenient stability indicator is the potential margin

$$\Delta E(pH) \;:=\; E_{\mathrm{pit}}(pH) - E_{\mathrm{oc}}(pH). \tag{5}$$

When ΔE is large and positive, the system operates comfortably below breakdown conditions; when ΔE decreases, breakdown becomes more likely. A smooth surrogate for breakdown risk is a logistic map

$$P_{\mathrm{bd}}(pH) \;=\; \frac{1}{1+\exp\big(\alpha\, \Delta E(pH)\big)}, \tag{6}$$

with $\alpha > 0$ governing sensitivity. This permits a process-window feasibility statement combining efficacy and stability:

$$\eta(n) \geq \eta_{\min}, \qquad m_{\mathrm{sub}}(n) \leq m_{\mathrm{allow}}, \qquad P_{\mathrm{bd}}(pH) \leq P_{\max}. \tag{7}$$

The qualitative observations that passive zones are destroyed more easily in acidic $KMnO_4$ than alkaline $KMnO_4$ correspond to a smaller ΔE (thus larger P_{bd}) in the acidic regime. The additional observation that very high alkalinity narrows the passive region corresponds to a regime where ΔE again decreases, producing the non-monotone "moderate-alkaline optimum" structure.

2.1.5 Scalarized decision objective.

When a single recommended operating point is needed, a scalarized objective can be formed. One convenient form penalizes corrosion and instability while rewarding efficacy:

$$J(pH, n) \;=\; w_1\big(1-\eta(n)\big) \;+\; w_2\frac{m_{\mathrm{sub}}(n)}{m_{\mathrm{allow}}} \;+\; w_3 P_{\mathrm{bd}}(pH), \tag{8}$$

with weights $w_1, w_2, w_3 \geq 0$ reflecting plant priorities. The process window corresponds to low-J regions that also satisfy the hard constraints in (7). This formulation makes explicit that "best" depends on allowed metal loss and acceptable breakdown probability, not only on oxide-removal speed.

2.2 Saturation kinetics for oxide removal on preoxidized 304L

2.2.1 Single-compartment inventory depletion model

For oxide-bearing specimens, oxide removal is inventory-limited. A minimal model assumes that, per cycle, a constant fraction of the remaining removable oxide is depleted. Let $M(n)$ denote the removable oxide mass remaining after n cycles. A discrete-time depletion law is

$$M(n) \;=\; (1-\phi)\,M(n-1), \qquad 0<\phi<1, \tag{9}$$

where ϕ is an effective per-cycle removal fraction that aggregates oxidant access, Cr(III)→Cr(VI) conversion efficiency, and reduction-step dissolution. Solving (9) gives

$$M(n) \;=\; M(0)\,(1-\phi)^n \;=\; M(0)\,e^{-kn}, \qquad k := -\ln(1-\phi) > 0. \tag{10}$$

The cumulative oxide-related mass removed after n cycles is then

$$m_{\mathrm{ox}}(n) \;=\; M(0) - M(n) \;=\; M(0)\big(1-e^{-kn}\big). \tag{11}$$

Identifying $m_\infty \equiv M(0)$ yields the compact saturation law

$$m_{\mathrm{ox}}(n) \;=\; m_\infty\left(1-e^{-kn}\right), \tag{12}$$

and therefore the normalized efficacy becomes

$$\eta(n) \;=\; \frac{m_{\mathrm{ox}}(n)}{m_\infty} \;=\; 1-e^{-kn}. \tag{13}$$

Eq. (13) gives an explicit cycle-count rule: to achieve $\eta(n) \geq \eta_{\min}$, one needs

$$n \;\geq\; \frac{1}{k}\ln\!\left(\frac{1}{1-\eta_{\min}}\right). \tag{14}$$

Thus, chemistry choices that increase k reduce the required cycle count for a given efficacy target.

2.2.2 Adding substrate loss as a separable term

To connect to observed total mass loss, a simple separable extension adds a substrate-loss component that grows approximately linearly with n when the substrate remains largely passive and each cycle has similar duration:

$$m(n) \;=\; m_\infty\big(1-e^{-kn}\big) \;+\; an, \tag{15}$$

where $a \geq 0$ is an effective per-cycle substrate dissolution term (mg/cm^2/cycle). Differencing (15) yields the per-cycle increment

$$\Delta m(n) \;:=\; m(n) - m(n-1) \;=\; m_\infty\big(1-e^{-k}\big)e^{-k(n-1)} \;+\; a. \tag{16}$$

Eq. (16) clarifies the diminishing-return structure: the oxide-driven increment decays geometrically with n, while a remains constant. When the oxide inventory is nearly exhausted, $\Delta m(n) \approx a$ and additional cycling becomes dominated by substrate loss rather than useful oxide removal.

2.2.3 Parameter identification from cycle data

If a is negligible or known, (12) can be linearized for estimation. Rearranging gives

$$1 - \frac{m_{\mathrm{ox}}(n)}{m_\infty} \;=\; e^{-kn}, \qquad \ln\!\left(1 - \frac{m_{\mathrm{ox}}(n)}{m_\infty}\right) \;=\; -kn. \tag{17}$$

If m_∞ is approximated from a near-plateau value and $m_{\mathrm{ox}}(n) \approx m(n)$ during oxide-dominated cycles, then an estimate of k can be computed from each n via

$$\widehat{k}(n) \;=\; -\frac{1}{n}\ln\!\left(1 - \frac{m(n)}{\widehat{m}_\infty}\right), \tag{18}$$

and then aggregated (e.g., averaged) across early cycles. When a is not negligible, (16) provides a route: if late-cycle increments approximate a, then subtracting a from early increments yields

$$\Delta m(n) - a \;=\; C\,e^{-k(n-1)}, \qquad C := m_\infty\big(1 - e^{-k}\big), \tag{19}$$

so that ratios satisfy

$$\frac{\Delta m(n+1) - a}{\Delta m(n) - a} \;=\; e^{-k}, \qquad k \;=\; -\ln\!\left(\frac{\Delta m(n+1) - a}{\Delta m(n) - a}\right). \tag{20}$$

In practical use, k is best identified by constrained nonlinear least squares on (15) with $m_\infty \geq 0$, $k > 0$, and $a \geq 0$, and then validated by checking whether late-cycle increments are close to a and whether the residuals are structureless.

2.2.4 Two-compartment extension for heterogeneous oxides

Real preoxidized films are heterogeneous, typically containing a more accessible fraction (outer porous oxides) and a less accessible fraction (inner Cr-rich barrier oxides). A mathematically simple but physically meaningful extension partitions the removable inventory into "fast" and "slow" compartments:

$$m(n) \;=\; m_f\big(1 - e^{-k_f n}\big) \;+\; m_s\big(1 - e^{-k_s n}\big) \;+\; an, \qquad k_f > k_s > 0, \tag{21}$$

where m_f and m_s are the removable inventories of each compartment. The corresponding efficacy is

$$\eta(n) \;=\; \frac{m_f\big(1 - e^{-k_f n}\big) + m_s\big(1 - e^{-k_s n}\big)}{m_f + m_s}. \tag{22}$$

This form captures rapid early removal driven by k_f and a slower tail driven by k_s, while still producing a strict plateau when inventories are depleted. In the process-window context, moderate alkalinity is expected to increase k_f (fast accessibility) without excessively increasing a or destabilizing passivity, whereas strong acidity may increase both k_f and a while also increasing breakdown probability through a reduced potential margin (5).

2.2.5 Diagnosing secondary effects at large cycle count

The saturation framework provides explicit signatures for secondary phenomena. If $m(n)$ continues to increase approximately linearly after oxide depletion, then a is significant and substrate dissolution dominates, implying that cycling beyond the saturation point should be avoided. If $m(n)$ departs from a monotone saturation trend, then reprecipitation or reoxidation may be occurring. Surface roughening and microspore formation can also alter effective kinetics by increasing reactive area; in such a case, k may appear to increase with n even when true oxide inventory is nearly exhausted. These diagnostics motivate joint interpretation of $m(n)$ with polarization indicators (i_{pass}, passive-region width, and breakdown tendencies) and morphology, ensuring that the selected process window is robust not only for immediate oxide removal but also for corrosion control and post-treatment surface stability.

3. Results: Quantitative Reanalysis of the Alkaline Dataset

3.1 Extracted cumulative mass loss and cycle-to-cycle increments

We focus on the preoxidized 304L dataset obtained under a moderate alkaline oxidizing step (0.4 g/L NaOH + 1 g/L $KMnO_4$), because it is the clearest example in the source study where oxide removal appears to converge rapidly with repeated oxidation–reduction cycling. The reported cumulative mass losses $m(n)$ after $n = 1, \ldots, 5$ cycles are reproduced in Table 2. Throughout this section, $m(n)$ denotes net areal mass loss (mg/cm^2) measured gravimetrically after completing the n-th oxidation–reduction cycle.

Table 2: Cumulative mass loss for preoxidized 304L under alkaline cycling (reported series).

Cycles n	1	2	3	4	5
$m(n)$ (mg/cm^2)	0.161	0.256	0.351	0.354	0.358

A more informative view is obtained by examining the marginal mass-loss increment per additional cycle,

$$\Delta m(n) \;:=\; m(n) - m(n-1), \qquad n \geq 2, \tag{23}$$

with $m(0) \equiv 0$ for convenience. The resulting increments are

$$\Delta m(1) = 0.161, \quad \Delta m(2) = 0.095, \quad \Delta m(3) = 0.095, \quad \Delta m(4) = 0.003, \quad \Delta m(5) = 0.004 \text{ mg/cm}^2.$$

These values demonstrate a sharp transition between an "active removal" regime (cycles 1–3) and a "near-plateau" regime (cycles 4–5). To quantify the extent of diminishing returns, we define the normalized cumulative removal fraction (relative to the final measured value at $n = 5$),

$$\eta_{\text{net}}(n) \;:=\; \frac{m(n)}{m(5)}. \tag{24}$$

Using $m(5) = 0.358$ mg/cm^2, we obtain

$$\eta_{\text{net}}(1) \approx 0.450, \quad \eta_{\text{net}}(2) \approx 0.715, \quad \eta_{\text{net}}(3) \approx 0.981, \quad \eta_{\text{net}}(4) \approx 0.989, \quad \eta_{\text{net}}(5) = 1.$$

Thus, approximately 98% of the observed net mass-loss outcome is achieved by $n = 3$ cycles, while cycles 4 and 5 contribute a combined additional net loss of only 0.007 mg/cm^2.

Because each cycle in the reported protocol contains 8 h oxidation + 5 h reduction, the cycle duration is $\tau_c = 13$ h. A simple net removal rate proxy for cycle n is therefore

$$r(n) \;:=\; \frac{\Delta m(n)}{\tau_c} \quad (\text{mg/cm}^2/\text{h}). \tag{25}$$

For cycles 2 and 3, $r(2) = r(3) \approx 0.095/13 \approx 7.31\times10^{-3}$ mg/cm^2/h, whereas for cycles 4 and 5, $r(4) \approx 2.31\times10^{-4}$ mg/cm^2/h and $r(5) \approx 3.08\times10^{-4}$ mg/cm^2/h. This order-of-magnitude reduction in marginal rate is precisely the quantitative signature expected when oxide inventory depletion and/or counteracting mass-gain processes dominate the later cycles.

3.2 Saturation-fit interpretation and parameter extraction

3.2.1 Baseline saturation model

A first-order representation of oxide-inventory-limited removal is the saturating form introduced earlier,

$$m_{\text{ox}}(n) = m_\infty \left(1 - e^{-kn}\right), \tag{26}$$

where m_∞ is the effective removable inventory and k is the effective per-cycle depletion constant. If the measured $m(n)$ were purely oxide-inventory depletion (with negligible substrate dissolution and negligible mass gain from reprecipitation), then one would expect $m(n) \approx m_{\text{ox}}(n)$ and therefore $m(n)$ would approach m_∞ monotonically.

A practical estimator of the plateau is the late-cycle mean,

$$\widehat{m}_\infty \;:=\; \frac{m(4) + m(5)}{2} = \frac{0.354 + 0.358}{2} = 0.356 \text{ mg/cm}^2, \tag{27}$$

with an empirical half-range uncertainty of approximately ± 0.002 mg/cm^2 across the last two points. Because $m(5)$ is slightly larger than $\widehat{m}_\infty$, we adopt a numerically stable conservative plateau $\widetilde{m}_\infty = 0.360$ mg/cm^2 for rate-constant calculations; this choice prevents singularities in logarithmic transforms and reflects that the true asymptote may lie marginally above the observed $n = 5$ value.

Under the constant-k assumption, Eq. (26) can be inverted to estimate k from each n:

$$\widehat{k}(n) \;=\; -\frac{1}{n} \ln\!\left(1 - \frac{m(n)}{\widetilde{m}_\infty}\right). \tag{28}$$

Using $\widetilde{m}_\infty = 0.360$ mg/cm^2, the resulting effective constants are

$$\widehat{k}(1) \approx 0.593, \quad \widehat{k}(2) \approx 0.621, \quad \widehat{k}(3) \approx 1.230, \quad \widehat{k}(4) \approx 1.024, \quad \widehat{k}(5) \approx 1.039 \quad \text{cycle}^{-1}.$$

The noticeable change between $\widehat{k}(1)$–$\widehat{k}(2)$ and $\widehat{k}(3)$ indicates that a *single constant* k is not sufficient to fully explain the observed sequence. This is not a weakness of the data; rather, it is a useful diagnostic that points to additional physics: either the effective accessibility of oxide increases after early cycles (activation/penetration effects), or later cycles are influenced by counteracting mass-gain processes (e.g., reoxidation or precipitation) that flatten the net mass-loss curve.

3.2.2 Activation-modulated depletion interpretation

A mathematically transparent way to represent a changing effective removal rate is to allow the "hazard" (cumulative depletion intensity) to evolve with cycle number. Define

$$K(n) \;:=\; -\ln\!\left(1-\frac{m(n)}{\widetilde{m}_\infty}\right), \tag{29}$$

so that the baseline saturation model corresponds to $K(n)=kn$ and, more generally, $K(n)=\sum_{j=1}^{n} k_j$ with cycle-dependent effective removal constants k_j. Using $\widetilde{m}_\infty = 0.360$ mg/cm^2, we obtain

$$K(1)\approx 0.593, \quad K(2)\approx 1.242, \quad K(3)\approx 3.689, \quad K(4)\approx 4.094, \quad K(5)\approx 5.193.$$

The implied cycle-wise intensities $k_n := K(n)-K(n-1)$ are therefore

$$k_1\approx 0.593, \quad k_2\approx 0.649, \quad k_3\approx 2.447, \quad k_4\approx 0.405, \quad k_5\approx 1.099.$$

The pronounced spike at cycle 3 is consistent with a threshold effect: after two cycles, transport pathways into the oxide (microcracks, pore opening, disruption of a Cr-rich barrier) may increase the chemically accessible fraction, causing a temporarily higher effective depletion intensity. The subsequent reduction in marginal mass loss after cycle 3 is consistent with depletion of the remaining accessible inventory and/or the onset of counteracting mass gain.

3.2.3 Including substrate dissolution and mass-gain countereffects

Because $m(n)$ is a *net* gravimetric measure, it can in principle be influenced by both dissolution and deposition. A minimal decomposition is

$$m(n) \;=\; m_{\mathrm{diss}}(n) - m_{\mathrm{gain}}(n), \tag{30}$$

where $m_{\mathrm{diss}}(n)$ includes oxide removal plus any substrate dissolution, and $m_{\mathrm{gain}}(n)$ captures net mass increases due to reprecipitation/reoxidation products. If $m_{\mathrm{diss}}(n)$ follows inventory-limited saturation while $m_{\mathrm{gain}}(n)$ becomes non-negligible only after a surface-state transition (e.g., after microspores form), then a near-plateau in $m(n)$ can occur even when dissolution continues, because the late-cycle net increment

$$\Delta m(n) \;=\; \Delta m_{\mathrm{diss}}(n) - \Delta m_{\mathrm{gain}}(n) \tag{31}$$

approaches zero when $\Delta m_{\mathrm{diss}}(n) \approx \Delta m_{\mathrm{gain}}(n)$. The reported morphology evidence of reoxidation after additional cycling is compatible with this mechanism and provides a physically grounded explanation for why the late-cycle net increments are so small.

3.2.4 Engineering stopping rule from the net saturation behavior

Irrespective of whether the plateau is driven purely by depletion or partially by counteracting mass gain, the dataset provides a robust operational conclusion: the marginal benefit of cycling beyond $n=3$ is extremely small. A quantitative stopping criterion can be defined by selecting a tolerance $\varepsilon \in (0,1)$ and choosing the smallest $n^\star$ such that

$$m(n^\star) \;\geq\; (1-\varepsilon)\, m(N), \tag{32}$$

where N is the maximum tested cycles (here $N=5$) or a proxy for the plateau. With $\varepsilon = 0.02$ and $m(N)=m(5)$, we obtain $m(3)=0.351 \geq 0.98\times 0.358 = 0.3508$, hence $n^\star = 3$. This rule is attractive because it is directly tied to measured outcomes and does not require strong model assumptions; it also aligns with the process-window philosophy of minimizing unnecessary corrosion exposure once decontamination performance has converged.

3.3 Surface-state consequence: microspores, area amplification, and reoxidation tendency

SEM observations in the source study indicate that oxide films are almost removed after approximately two cycles under moderate alkalinity, but microspores remain on the surface. From a mechanistic perspective, microspores and porous residual texture can influence post-treatment behavior through two coupled pathways: effective area amplification and nucleation facilitation.

A simple geometric surrogate for area amplification is the roughness/porosity surface-area factor $\mathcal{A} > 1$, defined as the ratio of true reactive area to projected geometric area. If microspores are approximated as hemispherical pits of mean radius r_p with areal number density ρ_p (pores per cm^2), then the excess area contributed by one pore is approximately $2\pi r_p^2$

(hemisphere surface area), while the projected footprint is πr_p^2. The true area per unit projected area can be approximated as

$$\mathcal{A} \;\approx\; 1 + \rho_p \left(2\pi r_p^2 - \pi r_p^2\right) \;=\; 1 + \rho_p \pi r_p^2. \tag{33}$$

Even modest values of $\rho_p r_p^2$ can therefore raise $\mathcal{A}$ above unity and increase the effective rate of interfacial reactions during subsequent exposure. In addition, porous features can reduce diffusion lengths for oxidizing species and provide micro-environments where local chemistry differs from the bulk, further accelerating oxide nucleation.

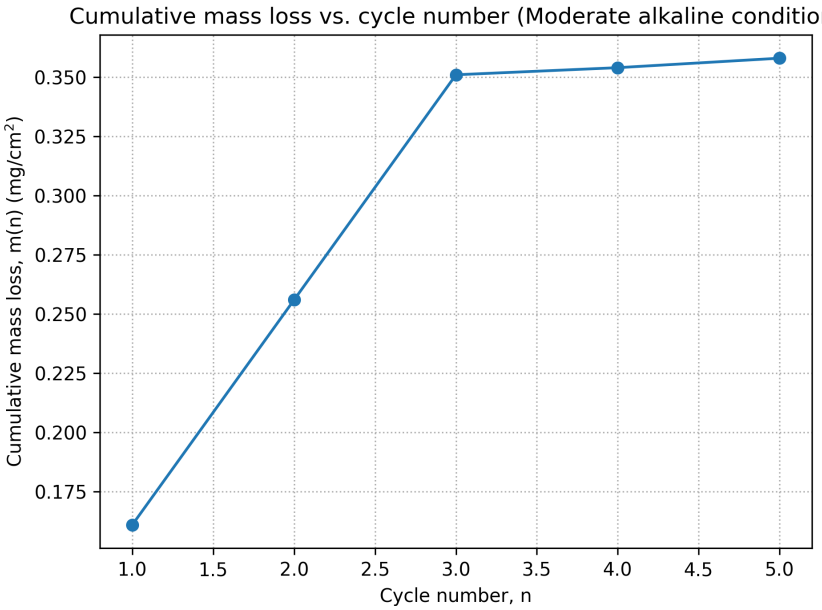

Figure 1: Cumulative mass loss $m(n)$ versus cycle number n for the moderate-alkaline condition, illustrating rapid convergence by $n \approx 3$.

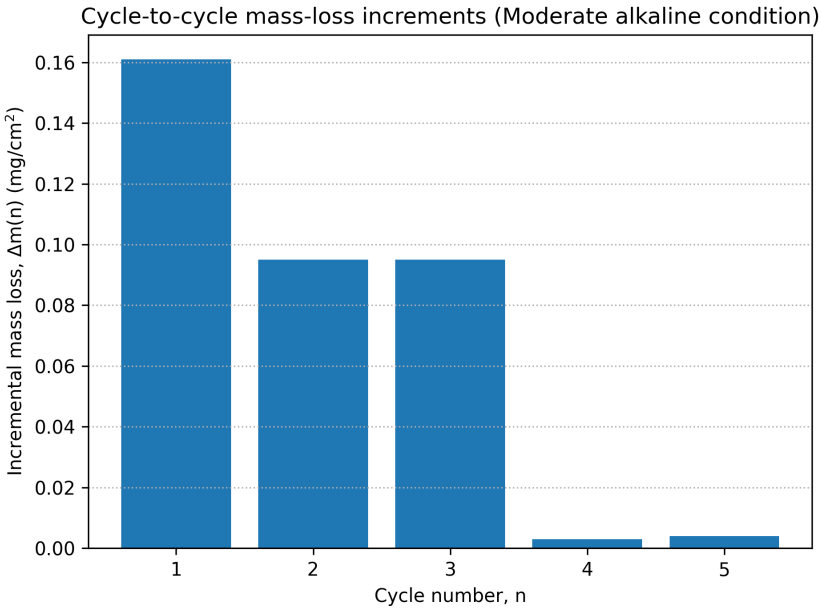

Figure 2: Cycle-to-cycle increments $\Delta m(n)$ highlighting the sharp reduction in marginal benefit after the third cycle.

A second pathway is nucleation facilitation. A standard expression for heterogeneous nucleation rate can be written as

$$J \;=\; J_0 \exp\!\left(-\frac{\Delta G^*}{k_B T}\right), \tag{34}$$

where ΔG^* is the nucleation barrier, k_B is Boltzmann's constant, and T is temperature. For heterogeneous nucleation on a surface, ΔG^* is reduced relative to homogeneous nucleation by a factor that depends on wetting and interfacial geometry; porous/rough surfaces effectively lower the barrier by providing favorable curvature, defect sites, and locally increased

adsorption. In practical terms, even a moderate reduction of ΔG^* leads to an exponential increase in J, making reoxidation during high-temperature aqueous service more likely on a microspore-rich surface. This provides a quantitative rationale for the reported observation that after additional cycling, reoxidation morphology becomes similar to the initial preoxidized surface upon subsequent exposure.

Taken together, the alkaline dataset implies that process design should treat cycle count as both a decontamination and a surface-state control variable. While cycles 1–3 deliver nearly all net oxide-removal benefit, additional cycles may unnecessarily condition the surface toward porosity and higher reoxidation susceptibility, without appreciable improvement in net mass-loss outcomes. This conclusion supports the broader process-window recommendation: operate in moderate alkalinity to preserve passivity, and terminate cycling at or near the saturation point defined by Eq. (32).

4. Discussion

The combined gravimetric, electrochemical, and morphological evidence supports the interpretation that moderate alkaline permanganate conditions offer a practically favorable compromise between deposit conditioning and substrate protection [14, 15]. From the efficacy perspective, permanganate provides sufficient oxidizing capacity to convert Cr(III) species within chromium-bearing oxides into more soluble, higher-valence forms that can be removed during the subsequent reducing step [16, 11]. From the corrosion-control perspective, 304L stainless steel relies on a Cr-enriched passive film, and the polarization observations indicate that this passive regime is more readily destabilized in acidic permanganate than in alkaline permanganate [17, 12]. Thus, moving from low pH to moderate alkaline pH shifts the system toward a regime where deposit oxidation remains effective while the passive film retains a wider stability range [18, 14].

This "moderate alkaline optimum" is consistent with a non-monotone dependence of corrosion risk on pH [13, 19]. In strongly acidic permanganate solutions, dissolution of protective film constituents and increased susceptibility to passive breakdown elevate both uniform and localized corrosion risk [12, 19]. Conversely, the reported observation that increasing NaOH concentration can narrow the passivation potential range indicates that extreme alkalinity is not benign: the passive domain can shrink and passivity may break down under sufficiently high alkalinity [20, 14]. This motivates an upper bound on NaOH addition and rejects any simplistic rule that greater alkalinity monotonically improves corrosion resistance [13]. Instead, pH should be treated as a tuning variable that simultaneously affects oxidant chemistry, oxide dissolution, and passive stability [18].

A useful way to formalize this point is through the potential margin $\Delta E(pH) = E_{\mathrm{pit}}(pH) - E_{\mathrm{oc}}(pH)$ introduced earlier. Acidification tends to reduce E_{pit} and may raise E_{oc} in strongly oxidizing environments, thereby shrinking ΔE and increasing breakdown probability [19]. Excessive alkalinity can also reduce ΔE by narrowing the passive region or lowering the breakdown threshold, again increasing breakdown probability [20]. The moderate alkaline regime is therefore interpreted as a region where ΔE is sufficiently positive to maintain passivity while oxidation chemistry remains effective for conditioning chromium-bearing oxides [17, 18].

A central quantitative outcome of the alkaline dataset is the sharp reduction in marginal net mass loss after approximately three cycles, indicating that most removable oxide inventory has been depleted and further cycling provides diminishing returns [21, 10]. In the saturation-kinetics framework, this corresponds to the regime where the oxide-driven increment $m_\infty(1 - e^{-k})e^{-k(n-1)}$ becomes small compared to any persistent per-cycle substrate dissolution a or compared to counteracting mass-gain processes (reoxidation/reprecipitation) [21]. Practically, this implies that extending the number of cycles beyond the saturation point consumes process time and corrosion allowance without materially improving the decontamination objective [22].

This logic can be formalized by defining a stopping tolerance ε and selecting the minimum $n^\star$ such that $m(n^\star) \geq (1 - \varepsilon)m_{\mathrm{plateau}}$ [22]. Once $n \geq n^\star$, the incremental oxide-removal benefit per cycle is small, and the procedure should terminate unless additional cycles are justified by independent evidence of persistent oxide coverage. Importantly, the "plateau" should be interpreted jointly with morphology [15]. If SEM indicates that oxide is almost removed by two cycles but microspores remain, then the process objective may already be met, and further cycles may be counterproductive by increasing porosity and conditioning the surface toward reoxidation susceptibility [23, 24].

The observation of microspores after oxide removal provides a mechanistic bridge between short-term decontamination efficacy and long-term surface stability [23]. Porous and roughened surfaces exhibit a higher true reactive area than a polished surface and supply defect-rich sites that lower the barrier for heterogeneous nucleation of new oxides during subsequent high-temperature water exposure [24]. In terms of the area factor $\mathcal{A}$, microspore formation increases effective interfacial area, thereby amplifying reaction fluxes during both oxidation and later service [24]. Additionally, if reoxidation occurs between cycles or after returning to service conditions, the net gravimetric signal may partially mask ongoing dissolution because $\Delta m(n) = \Delta m_{\mathrm{diss}}(n) - \Delta m_{\mathrm{gain}}(n)$ can approach zero even when both terms are non-negligible [21].

This strengthens the case for stopping at the earliest cycle count that satisfies oxide-removal requirements, rather than "over-cycling" in an attempt to gain marginal additional removal [22].

Taken together, the evidence suggests a practical rule-set for procedure design: choose an oxidizing-step pH in the moderate alkaline regime to balance deposit oxidation with passive stability; avoid strongly acidic permanganate unless deposit resistance necessitates it and corrosion allowances permit; avoid extreme alkalinity due to the observed shrinkage of passivity stability ranges; and terminate oxidation–reduction cycling at or near the saturation point inferred from cumulative mass loss and verified by morphology [14, 18, 20].

The present framework is intentionally structured so that it can be upgraded from a mechanistic reanalysis to a predictive engineering tool with a limited set of targeted additional measurements [25]. Three additions are particularly high-value because they directly identify the model parameters and validate the proposed causal chain from pH to passivity to removal saturation and reoxidation [25].

X-ray photoelectron spectroscopy (XPS), preferably combined with controlled sputter-depth profiling, can quantify the oxidation states and relative abundances of Fe, Cr, Ni, Mn, and O as a function of depth in the oxide/passive layers after each cycle and across pH regimes [26]. This directly tests the key mechanistic assumption that the oxidizing step converts Cr(III)-bearing oxide fractions into higher-valence, more soluble forms [16]. XPS also enables separation of deposit-oxide removal from passive-film modification by tracking Cr enrichment and chemical states near the alloy interface [26].

While polarization curves reveal passive ranges and breakdown tendencies, electrochemical impedance spectroscopy provides complementary quantitative separation of film resistance and capacitance evolution, enabling a more direct measure of passive-film integrity [25, 27]. A simple equivalent-circuit interpretation can extract a charge-transfer resistance R_{ct} and a film capacitance (or constant-phase element), allowing one to define a passivity robustness index.

To convert the qualitative SEM observation of microspores into a quantitative reoxidation-risk model, surface topography should be measured via 3D optical profilometry or atomic force microscopy (AFM) [23]. These techniques yield roughness parameters and enable estimation of an area amplification factor $\mathcal{A}$ that can be incorporated into reoxidation-risk constraints [24], for example

$$\mathcal{R} \;:=\; \frac{R_{ct}}{C_f}, \tag{35}$$

or alternative monotone indicators that correlate with barrier performance. Tracking $\mathcal{R}$ across pH and cycles would validate the hypothesized non-monotone stability trend and provide parameterization of the breakdown-risk surrogate $P_{\mathrm{bd}}(pH)$ via the potential margin ΔE and film robustness metrics.

To convert the qualitative SEM observation of microspores into a quantitative reoxidation-risk model, surface topography should be measured via 3D optical profilometry or atomic force microscopy (AFM). These techniques yield roughness parameters (e.g., R_a, R_q) and can be combined with SEM image analysis to estimate microspore size distributions and areal density. A measurable area amplification factor $\mathcal{A}$ can then be computed (or at least bounded) and incorporated into nucleation and growth proxies, linking porosity metrics to reoxidation tendency. In a predictive formulation, reoxidation risk can be parameterized as an increasing function of $\mathcal{A}$ and microspore density, and then used as an additional constraint in the process window:

$$\mathrm{ReoxidationRisk}(pH, n) \;\le\; R_{\max}. \tag{36}$$

With XPS, EIS, and topography measurements in place, the process-window framework can be implemented as an optimization over (pH, n) using the scalarized objective in Eq. (8) subject to constraints such as (7) and a reoxidation-risk bound. This would yield a procedure-selection tool that is not only consistent with observed mass-loss convergence but is also grounded in measured passive-film stability and quantified post-treatment surface condition.

5. Conclusions

A process-window and saturation-kinetics framework was developed for pH-controlled permanganate decontamination of 304L stainless steel. The reported trends support that acidic $KMnO_4$ is comparatively aggressive to 304L passivity, while moderate alkaline $KMnO_4$ achieves rapid oxide inventory depletion on preoxidized 304L with minimal benefit beyond approximately three cycles. The microspore morphology observed after oxide removal provides a plausible surface-state pathway for reoxidation, indicating that cycle count selection should be treated as both a corrosion and post-treatment reoxidation control variable. The framework can be strengthened into a predictive methodology via targeted surface-chemistry, impedance, and porosity measurements.

References

[1] Series, I. N. E. (2018). Status and trends in spent fuel and radioactive waste management. *IAEA Nuclear Energy Series No. NW-T-1.14 (Rev. 2)*

[2] EPRI. (2011). *Chemical Decontamination Guidelines*. EPRI Report 1022909, Electric Power Research Institute, Palo Alto, CA, 2011.

[3] Hewett, J. M. (2018). *Corrosion Film Solubility and Suspended Particle Behaviour of Corroding Ss316l Surfaces in Simulated Nuclear Plant Coolant* (Doctoral dissertation, University of Birmingham).

[4] Shang, Z. (2001). *A Study of Ag-110m in Aquatic and Terrestrial Ecosystems and the Development of a Radioecological Model*. HKU Theses Online (HKUTO).

[5] Trojanowicz, M., Intanin, A., Inpota, P., Chutimasakul, T., Tantirungrotechai, J., Wilairat, P., ... & Qiao, J.

[6] Little, E. A. (2006). Development of radiation resistant materials for advanced nuclear power plant. *Materials Science and Technology, 22*(5), 491-518.

[7] Fisher, K. B., Miller, B. D., Johns, E. C., & Marquis, E. A. (2018). The role of surface deformation in the oxidation response of type 304 SS in high temperature deaerated water. *Corrosion Science, 141,* 88-96.

[8] Hihara, L. H., Adler, R. P., & Latanision, R. M. (2013). *Environmental Degradation of Advanced and Traditional Engineering*. Chapter 29. Asphalt Pavement.

[9] Sedriks, A. J. (1996). *Corrosion of Stainless Steels*. John Wiley & Sons.

[10] Adams, V. D., Watts, R. J., & Pitts, M. E. (1986). Organics. *Journal (Water Pollution Control Federation), 58*(6), 449-471.

[11] Chen, L., Chamberlain, D. B., Conner, C., & Vandegrift, G. F. (1997). *A Survey of Decontamination Processes Applicable to DOE Nuclear Facilities* (No. ANL-97/19). Argonne National Lab.(ANL), Argonne, IL (United States).

[12] Marcus, P., & Oudar, J. (Eds.). (2002). *Corrosion Mechanisms in Theory and Practice* (pp. 243-286). New York: Marcel Dekker.

[13] Pourbaix, M. (1966). *Atlas of Electrochemical Equilibria in Aqueous Solutions*. NACE.

[14] Freire, L., Carmezim, M. J., Ferreira, M. G. S., & Montemor, M. F. (2011). The electrochemical behaviour of stainless steel AISI 304 in alkaline solutions with different pH in the presence of chlorides. *Electrochimica Acta, 56*(14), 5280-5289.

[15] Heusler, K. E. (1995). Passivity of metals and semiconductor. In *Materials Science Forum* (pp. 185-188).

[16] Mousty, C., & Walcarius, A. (2015). Electrochemically assisted deposition by local pH tuning: a versatile tool to generate ordered mesoporous silica thin films and layered double hydroxide materials. *Journal of Solid State Electrochemistry, 19*(7), 1905-1931.

[17] Olsson, C. O., & Landolt, D. (2003). Passive films on stainless steels—chemistry, structure and growth. *Electrochimica acta, 48*(9), 1093-1104.

[18] Macdonald, D. D. (1992). The point defect model for the passive state. *Journal of the Electrochemical Society, 139*(12), 3434.

[19] Mekki, A. (2003). *Effect of Particulate Impact on Oilfield Inhibitor*. The University of Manchester (United Kingdom).

[20] Heakal, F. E. T., Abd-Ellatif, W. R., Tantawy, N. S., & Taha, A. A. (2018). Impact of pH and temperature on the electrochemical and semiconducting properties of zinc in alkaline buffer media. *RSC Advances, 8*(7), 3816-3827.

[21] Guertin, J., Jacobs, J. A., & Avakian, C. P. (2004). *Chromium (VI) Handbook*. CRC press.

[22] Sotoodeh, K. (2020). Requirement and calculation of corrosion allowance for piping and valves in the oil and gas industry. *Journal of Bio-and Tribo-Corrosion, 6*(1), 21.

[23] Cao, L., Zhang, W., Jiang, C., Wang, H., An, H., Ye, C., ... & Deng, L. (2025). Effect of surface roughness on corrosion behaviour of stainless steel in supercritical CO2. *Journal of Materials Research and Technology, 36*(5,6), 4946-4954.

[24] Qu, M., Chen, H., Zhang, H., Jiao, S., & Xu, H. (2024). Insight Into the Effects of Environmental and Structural Factors on the Re-Oxidation of Cr (III) Hydroxides. *International Journal of Environmental Research, 18*(3), 39.

[25] Eguchi, K. (2021). *X-Ray Computed Tomography of Environmentally-Assisted Cracking in Lean Duplex Stainless Steel*. The University of Manchester (United Kingdom).

[26] Biesinger, M. C., Payne, B. P., Grosvenor, A. P., Lau, L. W., Gerson, A. R., & Smart, R. S. C. (2011). Resolving surface chemical states in XPS analysis of first row transition metals, oxides and hydroxides: Cr, Mn, Fe, Co and Ni. *Applied Surface Science, 257*(7), 2717-2730.

[27] Orazem, M. E., & Tribollet, B. (2008). Electrochemical impedance spectroscopy. *New Jersey, 1*(906), 383-389.